

# Design methodology of piezoelectric energy-harvesting skin using topology optimization

A. Takezawa · M. Kitamura · S. L. Vatanabe · E. C. N. Silva

Received: date / Accepted: date

**Abstract** This paper describes a design methodology for piezoelectric energy harvesters that thinly encapsulate the mechanical devices and exploit resonances from higher-order vibrational modes. The direction of polarization determines the sign of the piezoelectric tensor to avoid cancellations of electric fields from opposite polarizations in the same circuit. The resultant modified equations of state are solved by finite element method (FEM). Combining this method with the solid isotropic material with penalization (SIMP) method for piezoelectric material, we have developed an optimization methodology that optimizes the piezoelectric material layout and polarization direction. Updating the density function of the SIMP method is performed based on sensitivity analysis, the sequential linear programming on the early stage of the optimization, and the phase field method on the latter stage of the optimization to obtain clear optimal shapes without intermediate density. Numerical examples are provided that illustrate the validity and utility of the proposed method.

## 1 Introduction

Vibration-based energy-harvesting technologies have a tremendous amount of potential in various engineering fields. The devices derive electrical energies by scavenging from waste mechanical vibration energies. Such devices are expected to provide maintenance-free power sourcing for small electrical devices such as wireless sensors. This kind of technology can lead to new systems for monitoring structural health or implementing electrical medical devices. Vibration-based energy harvesting can be achieved by three different mechanisms: electromagnetic, electrostatic and piezoelectric. Among these, piezoelectric research is the more active field over the past decade. Summaries of the related research and applications can be found in several review articles (Sodano et al., 2004; Beeby et al., 2006; Priya, 2007; Anton and Sodano, 2007; Cook-Chennault et al., 2008).

The piezoelectric energy harvester is constructed usually of a piezoelectric material with additional masses located on a base structure. If a vibration has the same frequency as an eigen-frequency of the device, the device resonates and the piezoelectric material becomes highly deformed. Dynamic mechanical stress develops and a polarization occurs in the piezoelectric material. A dynamic electric field and an accompanying electric potential produces an output voltage across attached electrodes of the device. Several types of base structures have been proposed, such as cantilevers, cylinders, and clamped curved plates. The operation of the device exploits its fundamental mode because of its mechanical simplicity and clarity. In particular, the mechanical model for the fundamental vibrational mode of cantilever-type devices has been well established (Roundy et al.; duToit et al., 2005; Erturk and Inman, 2008b). However, to achieve higher energy-harvesting perfor-

---

A. Takezawa · M. Kitamura  
Division of Mechanical Systems and Applied Mechanics  
Institute of Engineering, Hiroshima University,  
1-4-1 Kagamiyama, Higashi-hiroshima, Hiroshima 739-8527,  
Japan  
Tel.: +81-82-424-7544  
Fax: +81-82-422-7194  
E-mail: akihiro@hiroshima-u.ac.jp  
E-mail: kitamura@hiroshima-u.ac.jp

S. L. Vatanabe and E. C. N. Silva  
Department of Mechatronics and Mechanical  
Systems Engineering,  
Escola Politécnica da Universidade de São Paulo,  
Av. Prof. Mello Moraes, 2231, São Paulo,  
SP 05508-900, Brazil  
E-mail: sandro.vatanabe@gmail.com  
E-mail: ecnsilva@usp.br

mances, devices exploiting higher vibrational modes were also researched. Erturk et al. studied theoretical and experimental aspects in cantilever-type devices (Erturk and Inman, 2008a; Erturk et al., 2009). Lee, Youn, and Jung proposed such devices to exploit multi-modal frequencies (Lee et al., 2009). Tadesse, Zhang and Priya developed a multi-physical multimodal energy harvester by combining piezoelectric and electromagnetic devices (Tadesse et al., 2009). Bourisli studied the optimal piezoelectric material location in higher vibrational modes in cantilever-type devices (Bourisli and Al-Ajmi, 2010). Lee and Youn developed a new energy harvesting concept they named “energy harvesting skin”, which uses the vibrations of the outer shell of vehicles or plants devices (Lee and Youn, 2011). In a more innovative manner, Gonnella, To, and Liu used isolated vibrations resulting from bandgap effects of the base structure to energy harvesting (Gonnella et al., 2009).

Recently, topology optimization (Bendsøe and Kikuchi, 1988; Bendsøe and Sigmund, 2003) has greatly assisted the development of piezoelectric energy harvesting devices because it enables a fundamental shape optimization of piezoelectric material subject to changes in topology. Zheng, Chang, and Gea first studied this topic in finding the optimal shapes of piezoelectric layers under static loads (Zheng et al., 2009). Rupp et al. developed an optimization method for not only the piezoelectric layer but also the electrode layer and mass layer under forced vibrations (Rupp et al., 2009). Chen et al. used the level-set method (Wang et al., 2003; Allaire et al., 2004) which is a type of topology optimization for cylindrical-type energy harvesters subject to axial forced vibrations (Chen et al., 2010). Nakasone and Silva used the piezoelectric material with penalization and polarization (PEMAP-P) method (Kögl and Silva, 2005), which optimizes simultaneously the shape of the piezoelectric layer and the poling direction to adjust the resonance mode shape of the device to an ideal setting (Nakasone and Silva, 2010). Sun and Kim developed an optimization method for an energy harvester using a magneto-electro-elastic laminate composed of piezoelectric and piezomagnetic materials (Sun and Kim, 2010). Kim et al. considered the effects of some of the parameters of topology optimization in their designs of energy harvesters (Kim et al., 2010).

Although the research has contributed to the development of novel energy harvesting devices, there still remain some technical challenges to address. The simultaneous optimization of the polarization direction and the layout of the piezoelectric material is one of these. In designing energy harvesting devices with multi-node vibration resonances (Lee and Xie, 2009; Tadesse et al., 2009; Bourisli and Al-Ajmi, 2010; Lee and Youn, 2011),

adjusting the poling direction of piezoelectric materials appropriately is very important in avoiding cancellation of the electric fields from opposite polarization directions. A few design examples were studied in the papers (Rupp et al., 2009; Nakasone and Silva, 2010) by suitably setting the sign of the piezoelectric tensor to depend on design variables and updating the variables using gradient-based optimization methods. However, if the shape of the piezoelectric material and poling direction are simultaneously optimized, the poling direction strongly affects the piezoelectric material optimization in each iteration. Thus, this type of optimization might encounter local optima; in other words, the problem might have a strong initial dependency. To avoid such problems, a double-loop optimization of the material layout and the poling direction is developed although the issue of computational overheads strongly persists. In contrast, the methodology to decide poling direction according to criteria based on the state of the device has been proposed (Lee and Youn, 2011). Lee and Youn segmented the piezoelectric plate and found the optimal poling direction through their optimization based on the phase of the electric voltage. However, because they had not tried topology optimization of piezoelectric material, the single-loop optimization methodology for the design problem of a piezoelectric material layout and its poling direction is an open problem.

In this paper, we focus on optimizing the vibration energy from energy harvesters and specifically poling. A d31-mode energy harvester using higher-order vibration modes is composed of a base-plate and a piezoelectric material sandwiched between a pair of electrodes. The poling direction for such harvesters is simply determined by the direction of stress applied to the material. That is, the sign of the piezoelectric tensor is established by the direction of polarization. The modified equations of state are solved by finite element method (FEM). Combining this methodology with conventional topology optimization and a phase field method (PFM) (Takezawa et al., 2010) for piezoelectric materials, we can implement design optimizations of piezoelectric materials and their polarization directions. This paper is organized as follows: a dynamic piezoelectric problem is first considered. The direction of poling is then set depending on the direction of the resultant polarization. The optimization problem is then formulated, viz. maximizing the electromechanical coupling factor. The proposed optimization methodology is implemented by the commonly-used SIMP method of topology optimization. The relationship between the physical properties of the piezoelectric material and the density function is defined and the sensitivity of the objective function with respect to the density function is calculated. The

density function is updated using the sequential linear programming (SLP) in the early stage of the optimization. In the latter stage of the optimization, the PFM updates the density function to obtain clear optimal shapes without intermediate densities. We provide numerical examples to illustrate the validity and utility of the proposed methodology.

## 2 Formulation

### 2.1 Modifying equations of state

To begin we consider the equations of state pertaining to the dynamic piezoelectric effect (Landau et al., 1984) in the domain  $\Omega$  composed of piezoelectric and base-structure domains  $\Omega_p$  and  $\Omega_b$  respectively. In ignoring time-dependent effects, only the equilibrium state needs consideration in the frequency domain. First, we assume no body forces in the dynamic problem and solutions to the forced vibration problem of the form  $e^{i\omega_{\text{input}}t}\mathbf{u}$  representing the periodic displacements. The balance of forces in the solid and Gauss's law are expressed as follows

$$\begin{cases} -\nabla \cdot \boldsymbol{\sigma}(\mathbf{u}) = \omega_{\text{input}}^2 \rho \mathbf{u} \\ \mathbf{u} = \mathbf{0} \text{ on } \Gamma_u \end{cases} \quad (1)$$

$$\begin{cases} -\nabla \cdot \mathbf{D}(V) = 0 \\ V = 0 \text{ on } \Gamma_V \end{cases} \quad (2)$$

where  $\boldsymbol{\sigma}$  is the stress tensor,  $\mathbf{u}$  the displacement vector,  $\omega_{\text{input}}$  the driving frequency,  $\mathbf{D}$  is the electric displacement vector,  $V$  the electric potential and  $\Gamma_u$  and  $\Gamma_V$  are boundaries for  $\mathbf{u}$  and  $V$  respectively on which Dirichlet boundary conditions are imposed. All eigenfrequencies of the above equation are assumed non-repeated.  $\boldsymbol{\sigma}$  and  $\mathbf{D}$  are formulated as follows:

$$\boldsymbol{\sigma} = \mathbf{C}\boldsymbol{\varepsilon} - \mathbf{e}^T \mathbf{E} \quad (3)$$

$$\mathbf{D} = \mathbf{e}\boldsymbol{\varepsilon} + \boldsymbol{\epsilon}_S \mathbf{E} \quad (4)$$

where  $\boldsymbol{\varepsilon}$  is the strain tensor,  $\mathbf{E}$  the electric field vector,  $\mathbf{C}$  the elastic tensor,  $\mathbf{e}$  the piezoelectric tensor, and  $\boldsymbol{\epsilon}_S$  the permittivity tensor. Using the displacement vector  $\mathbf{u}$  and electric potential  $V$ ,  $\boldsymbol{\varepsilon}$  and  $\mathbf{E}$  are defined as:

$$\boldsymbol{\varepsilon} = \frac{1}{2} (\nabla \mathbf{u} + (\nabla \mathbf{u})^T) \quad (5)$$

$$\mathbf{E} = -\nabla V \quad (6)$$

Equations (1)-(6) represent the mutual dependence of state variables  $\mathbf{u}$  and  $V$  in the piezoelectric problem.

The above-mentioned energy harvester using the d31 mode becomes the design object under consideration. The simple models of this type are shown in Figure

1(a). The direction of polarization depends on the direction of in-plane stress applied to the piezoelectric material. Depending on the base-plate deformation, the direction of stress can be different in the piezoelectric material. The polarization directions will also be different in the piezoelectric material as shown in Figure 1(b). Since the piezoelectric material is sandwiched between electrodes, the electric field established by these polarizations approximately cancel each other resulting in a very small field between these electrodes. To prevent cancellations, the piezoelectric material needs to be separated on the nodes of vibration with poling direction properly constructed at the fabrication stage to unify the direction of polarization in the circuit, as shown in Figure 1(c). Another way is that the circuit should be constructed on each part of the piezoelectric layer (Kim et al., 2005a,b).

Figure 1 is about here.

Finding the optimal poling directions is the preserve of piezoelectric actuator design optimization. The basic method to construct an optimal circuit is to set the design variable that determines the sign of piezoelectric tensor and optimize it (Kögl and Silva, 2005). In designing piezoelectric actuators or energy harvesters with complicated shapes, the optimal circuit construction is certainly hard to find without solving non-linear optimization problem. However, in the case of energy harvesters operating in the d31 mode as shown in Figure 1(b), the circuit design concept is analytically explained as shown in Figure 1(c). Since the direction of polarization depends on the direction of in-plane stress applied to the piezoelectric material, the poling direction should be changed according to the direction of the applied stress. In this research, we implement this procedure to the equations of state and find optimal poling direction by solving the modified equations of state as follows:

$$\boldsymbol{\sigma} = \mathbf{C}\boldsymbol{\varepsilon} - \mathbf{e}_s^T \mathbf{E} \quad (7)$$

$$\mathbf{D} = \mathbf{e}_s \boldsymbol{\varepsilon} + \boldsymbol{\epsilon}_S \mathbf{E} \quad (8)$$

where

$$\mathbf{e}_s = s \mathbf{e} \quad (9)$$

$$s = \frac{e\varepsilon_z}{|e\varepsilon_z|} \quad (10)$$

where  $s$  is a variable depending on the polarization direction,  $\mathbf{e}$  the original piezoelectric tensor and  $e\varepsilon_z$  is  $z$ -element of the polarization term  $\mathbf{e}\boldsymbol{\varepsilon}$ . These modified

state equations can be regarded as non-linear equations now parameterized by the value of the state-dependent coefficient  $s$ . The distribution of  $s$  at the converged state represents the optimal poling directions.

For solving by FEM, the above modified equations of state are represented in the weak form:

$$-m(\mathbf{u}, \mathbf{v}) + a(\mathbf{u}, \mathbf{v}) - b(\mathbf{v}, V) = L_m(\mathbf{v}) \quad (11)$$

$$b(\mathbf{u}, w) + c(V, w) = L_e(w) \quad (12)$$

with

$$m(\mathbf{u}, \mathbf{v}) = \omega_{\text{input}}^2 \int_{\Omega} \rho \mathbf{u} \mathbf{v} dx \quad (13)$$

$$a(\mathbf{u}, \mathbf{v}) = \int_{\Omega} \boldsymbol{\varepsilon}(\mathbf{u})^T \mathbf{C} \boldsymbol{\varepsilon}(\mathbf{v}) dx \quad (14)$$

$$b(\mathbf{u}, w) = \int_{\Omega} \boldsymbol{\varepsilon}(\mathbf{u})^T \mathbf{e}_s \mathbf{E}(w) dx \quad (15)$$

$$c(V, w) = \int_{\Omega} \mathbf{E}(V)^T \boldsymbol{\epsilon} \mathbf{E}(w) dx \quad (16)$$

$$L_m(\mathbf{v}) = \int_{\Gamma_m} \mathbf{t} \mathbf{v} ds \quad (17)$$

$$L_e(w) = \int_{\Gamma_e} \sigma w ds, \quad (18)$$

where  $\mathbf{v}$  and  $w$  are test functions,  $\mathbf{t}$  represent the tractions on  $\Gamma_m$ , and  $\sigma$  the surface charges on  $\Gamma_e$ . During optimization, we fix  $\Gamma_m$  and  $\Gamma_e$  independently of the values of the design variables.

## 2.2 Objective function

The objective function of the optimization problem is the electromechanical coupling coefficient  $k$  defined as follows (Berlincourt et al., 1964):

$$k^2 = \frac{E_{em}^2}{E_e E_m} = \frac{b(\mathbf{u}, V)^2}{a(\mathbf{u}, \mathbf{u}) c(V, V)} \quad (19)$$

where  $E_{em}$ ,  $E_e$ , and  $E_m$  are the electromechanical energy, the electrical energy and the mechanical (strain) energy respectively. If no charges lie on the boundary, substituting Equation (12) into Equation (19),  $k$  is simplified as follows:

$$k = \frac{E_e}{E_m} \quad (20)$$

Finally, we define the minimization of the inverse of  $k$  as the objective function in optimizing the piezoelectric domain  $\Omega_p$ ,

$$\text{minimize}_{\Omega_p} \frac{1}{k} = \frac{E_m}{E_e}. \quad (21)$$

## 2.3 Topology optimization

To optimize the geometry of  $\Omega_p$ , we used topology optimization method as this can perform more fundamental optimizations over arbitrary domains including shape and topology, as specified by the number of holes. The fundamental idea is to introduce a fixed, extended design domain  $D$  that includes, *a priori*, the optimal shape  $\Omega_{\text{opt}}$  and the utilization of the following characteristic function:

$$\chi(\mathbf{x}) = \begin{cases} 1 & \text{if } \mathbf{x} \in \Omega_{\text{opt}} \\ -1 & \text{if } \mathbf{x} \in D \setminus \Omega_{\text{opt}} \end{cases} \quad (22)$$

Using this function, the original design problem for  $\Omega$  is replaced by a material distribution problem incorporating a physical property,  $\chi A$ , in the extended design domain  $D$ , where  $A$  is a physical property of the original material comprising  $\Omega$ . Unfortunately, the optimization problem does not have any optimal solutions (Allaire, 2001). A homogenization method is used to perform the relaxation of the solution space (Bendsøe and Kikuchi, 1988; Allaire, 2001). In this way, the original material distribution optimization problem with respect to the characteristic function is replaced by an optimization problem of the “composite” consisting of the original material and a very weak material mimicking voids with respect to the density function. This density function represents the volume fraction of the original material and can be regarded as a weak limit of the characteristic function. In optimization problems, the relationship between the material properties of the composite and the density function must be defined. We use here one of the more popular ways, the “solid isotropic material with penalization” (SIMP) method, which introduces a completely artificial material property (Bendsøe, 1989; Bendsøe and Sigmund, 1999; Zhou and Rozvany, 1991). In this method, quantities relating the three material properties of the composite used in thermoelectric analysis, *viz.* elastic tensor  $\mathbf{C}$ , piezoelectricity tensor  $\mathbf{e}$ , permittivity tensor  $\boldsymbol{\epsilon}$ , and density  $\rho$ , are set as functions of the density of the penalization material  $\phi$ :

$$\mathbf{C}^* = \phi^{p_C} \mathbf{C}_0 \quad (23)$$

$$\mathbf{e}^* = \phi^{p_e} \mathbf{e}_0 \quad (24)$$

$$\boldsymbol{\epsilon}^* = \phi^{p_\epsilon} \boldsymbol{\epsilon}_0 \quad (25)$$

$$\rho^* = \phi^{p_\rho} \rho_0 \quad (26)$$

$$0 < \phi \leq 1, \quad (27)$$

where the upper suffix  $*$  signifies that the material property relates to the composite, the lower suffix  $_0$  to the original material, and  $p_C$ ,  $p_e$ ,  $p_\epsilon$ , and  $p_\rho$  are exponents introduced as positive penalization parameters. The above

density function is defined only over domain  $\Omega_p$  which determines  $D$  in Equation (22).

Finally, the optimization problem with the addition of a volume constraint is formulated as follows:

$$\underset{\phi}{\text{minimize}} \frac{1}{k} = \frac{E_m}{E_e} \quad (28)$$

and

$$\int_{\Omega_p} \phi dx \leq U_V \quad (29)$$

where  $U_V$  is the upper limit of the volume.

## 2.4 Sensitivity analysis

To perform optimizations, we used the SLP technique, which requires first-order sensitivity analysis of the objective function with respect to the design variable  $\phi$ . Since the derivation is lengthy, only the results are shown here and the detailed derivation is outlined in the Appendix.

The two adjoint variables  $\mathbf{p}$  and  $q$  are introduced to evaluate the sensitivity of the objective function which depends on the two state variables  $\mathbf{u}$  and  $V$ . The sensitivity of the objective function with respect to function  $\phi$  is represented as an independent type of objective function:

$$\begin{aligned} J'(\phi) = & -\omega_{\text{input}}^2 \rho'(\phi) \mathbf{u} \mathbf{p} + \boldsymbol{\varepsilon}(\mathbf{u})^T \mathbf{C}'(\phi) \boldsymbol{\varepsilon}(\mathbf{p}) \\ & - \boldsymbol{\varepsilon}(\mathbf{p})^T \mathbf{e}'_s(\phi) \mathbf{E}(V) + \boldsymbol{\varepsilon}(\mathbf{u})^T \mathbf{e}'_s(\phi) \mathbf{E}(q) \\ & - \mathbf{E}(V)^T \boldsymbol{\varepsilon}'(\phi) \mathbf{E}(q). \end{aligned} \quad (30)$$

where  $\mathbf{p}$  and  $q$  are adjoint variables which depends on the objective function.

The sensitivity of the electrochemical coupling factor  $k$  is calculated as follows:

$$k'(\phi) = \left( \frac{E_m}{E_e} \right)' = \frac{E'_m(\phi) E_e - E_m E'_e(\phi)}{E_e^2} \quad (31)$$

To calculate the sensitivity of the mechanical energy  $a(\mathbf{u}, \mathbf{u})$ , the adjoint variables  $\mathbf{p}$  and  $q$  must be obtained by solving the following coupled adjoint equations:

$$\begin{cases} -m(\mathbf{v}, \mathbf{p}) + a(\mathbf{v}, \mathbf{p}) + b(\mathbf{v}, q) = -2a(\mathbf{u}, \mathbf{v}) \\ \mathbf{p} = 0 \text{ on } \Gamma_u \end{cases} \quad (32)$$

$$\begin{cases} -b(\mathbf{p}, w) - c(q, w) = 0 \\ q = 0 \text{ on } \Gamma_V \end{cases} \quad (33)$$

and similarly for the mechanical energy  $c(V, V)$ :

$$\begin{cases} -m(\mathbf{p}, \mathbf{v}) + a(\mathbf{p}, \mathbf{v}) + b(\mathbf{v}, q) = 0 \\ \mathbf{p} = 0 \text{ on } \Gamma_u \end{cases} \quad (34)$$

$$\begin{cases} b(\mathbf{p}, w) + c(q, w) = 2c(V, w) \\ q = 0 \text{ on } \Gamma_V. \end{cases} \quad (35)$$

## 3 Numerical Implementation

### 3.1 Algorithm

The optimization procedure is performed using an algorithm incorporating the sensitivity calculation and updating the design variable using SLP and PFM (Takezawa et al., 2010). SLP is used at the early stage of the optimization with the so-called density filter (Bruns et al., 2002). PFM is used at the latter stage of the optimization to obtain clear optimal shapes without intermediate densities. The optimization algorithm is shown in figure 2.

Figure 2 is about here.

### 3.2 Discretization for FEM

FEM is used in this study to solve the modified equations of state. The internal approximations of the weak form of the modified equations of state in Equations (11)-(18) are first formulated as follows:

$$-m(\mathbf{u}_h, \mathbf{v}_h) + a(\mathbf{u}_h, \mathbf{v}_h) - b(\mathbf{v}_h, V_h) = L_m(\mathbf{v}_h) \quad (36)$$

$$b(\mathbf{u}_h, w_h) + c(V_h, w_h) = L_e(w_h). \quad (37)$$

The lowered suffix  $h$  indicates the discretized values. For simplicity, the discretized value of the state variables are approximated using the shape functions  $N_j$  of the first-order Lagrange finite elements corresponding to  $j$ -th nodes in accord with the following:

$$\mathbf{u}_h(\mathbf{x}) = \sum_{j=1}^{Nd} N_j(\mathbf{x}) \mathbf{u}_h(\mathbf{x}_j) \quad (38)$$

$$V_h(\mathbf{x}) = \sum_{j=1}^{Nd} N_j(\mathbf{x}) V_h(\mathbf{x}_j), \quad (39)$$

where  $\mathbf{x}_j$  is the position of  $j$ -th node. Finally, by combining the state equations into one equation and introducing the discretized test functions  $\mathbf{v}(\mathbf{x}) = \sum_{j=1}^{Nd} N_j(\mathbf{x}) = \sum_{j=1}^{Nd} N_j(\mathbf{x}) \{1 \ 1 \ 1\}^T$  and  $w(\mathbf{x}) = \sum_{j=1}^{Nd} N_j(\mathbf{x})$ , the weak-form equations of state can be formulated in their vector and matrix form:

$$(\mathbf{M} + \mathbf{K})\mathbf{U} = \mathbf{b} \quad (40)$$

where

$$\mathbf{M} = \begin{bmatrix} -\mathbf{M}_{uu} & 0 \\ 0 & 0 \end{bmatrix} \quad (41)$$

$$\mathbf{K} = \begin{bmatrix} \mathbf{K}_{uu} & -\mathbf{K}_{uV} \\ \mathbf{K}_{uV}^T & \mathbf{K}_{VV} \end{bmatrix} \quad (42)$$

$$\mathbf{M}_{uu} = [m(N_j, N_i)]_{1 \leq i, j \leq N_d} \quad (43)$$

$$\mathbf{K}_{uu} = [a(N_j, N_i)]_{1 \leq i, j \leq N_d} \quad (44)$$

$$\mathbf{K}_{uV} = [b(N_j, N_i)]_{1 \leq i, j \leq N_d} \quad (45)$$

$$\mathbf{K}_{VV} = [c(N_j, N_i)]_{1 \leq i, j \leq N_d} \quad (46)$$

$$\mathbf{U} = \begin{Bmatrix} \mathbf{U}_h \\ \mathbf{V}_h \end{Bmatrix} = \begin{Bmatrix} \{\mathbf{u}_h(\mathbf{x}_j)\}_{1 \leq j \leq N_d} \\ \{\mathbf{V}_h(\mathbf{x}_j)\}_{1 \leq j \leq N_d} \end{Bmatrix} \quad (47)$$

$$\mathbf{b} = \begin{Bmatrix} \{L_m(N_i)\}_{1 \leq i \leq N_d} \\ \{L_e(N_i)\}_{1 \leq i \leq N_d} \end{Bmatrix}. \quad (48)$$

Since the discretized equation of state in (40) is non-linear resulting from the dependency of the coefficients on the state variables, an iterative approach must be used to obtain solutions. We have used the residual minimization approach based on the Newton-Raphson method (Belytschko et al., 2000) whereby the residual for Equation (40) is defined as:

$$\mathbf{R} = (\mathbf{R}_u, \mathbf{R}_V) = (\mathbf{M} + \mathbf{K})\mathbf{U} - \mathbf{b}. \quad (49)$$

The updating of the discretized state vector at the  $n$ -th iteration  $\mathbf{U}^n$  is obtained from

$$\mathbf{U}^{n+1} = \mathbf{U}^n + \Delta \mathbf{U}^n = \mathbf{U}^n - \left( \frac{\partial \mathbf{R}(\mathbf{U}^n)}{\partial \mathbf{U}} \right)^{-1} \mathbf{R}(\mathbf{U}^n). \quad (50)$$

The increment  $\Delta \mathbf{U}^n$  is calculated by solving the following linear system:

$$\frac{\partial \mathbf{R}(\mathbf{U}^n)}{\partial \mathbf{U}} \Delta \mathbf{U}^n = -\mathbf{R}(\mathbf{U}^n), \quad (51)$$

with the tangent matrix  $\frac{\partial \mathbf{R}(\mathbf{U}^n)}{\partial \mathbf{U}}$  evaluated as follows:

$$\frac{\partial \mathbf{R}(\mathbf{U}^n)}{\partial \mathbf{U}} = \begin{bmatrix} \frac{\partial \mathbf{R}_u}{\partial \mathbf{U}_h} & \frac{\partial \mathbf{R}_u}{\partial \mathbf{V}_h} \\ \frac{\partial \mathbf{R}_V}{\partial \mathbf{U}_h} & \frac{\partial \mathbf{R}_V}{\partial \mathbf{V}_h} \end{bmatrix}. \quad (52)$$

Because the derivatives of the variable  $s$  in Equation (10) vanish, the tangent matrix as a result equals  $\mathbf{M} + \mathbf{K}$ . Note that, the converged non-linear state equations are slow to converge as the solution oscillates due to the varying sign of the piezoelectric coefficient. Thus, the Newton-Raphson calculation is performed with specified iteration times, but is sufficient to obtain optimal poling direction.

The adjoint equations in Equations (32)-(35) are also solved by FEM. Note that the modified piezoelectric tensor is independent of adjoint variables  $\mathbf{p}$  and  $\mathbf{q}$ . Thus, these adjoint equations are linear and the solutions can be obtained without any iterations.

### 3.3 Phase field method for shape optimization

PFM for shape optimization (Takezawa et al., 2010), which is used in the latter stage of the optimization procedure, is outlined. The method uses the identical domain representation and sensitivity analysis as the density function with the SIMP-based topology optimization. Different from the ordinary SIMP, for which the design variable is updated by the gradient based optimization method, the density function is updated by solving the following PDE so-called Allen-Cahn equation in the PFM.

$$\frac{\partial \phi}{\partial t} = \kappa \nabla^2 \phi - f'(\phi) \quad (53)$$

with

$$f(\phi) = \frac{1}{4}w(\phi) + \eta \frac{J'(\phi)}{\|J'(\phi)\|} g(\phi) \quad (54)$$

$$w(\phi) = \phi^2(1 - \phi^2) \quad (55)$$

$$g(\phi) = \phi^3(6\phi^2 - 15\phi + 10) \quad (56)$$

where  $t$  is the artificial time corresponding to the step size of the design variable,  $f$  is the asymmetric double well potential sketched in Figure 3, and  $\eta$  is a positive coefficient. Note  $f$  has two minimums on 0 and 1. Because of couplings between diffusion and reaction terms in Equation (53), the density function  $\phi$  is divided into several domains corresponding to the value 0 or 1. The so-called phase field interface corresponding to the intermediate values  $0 < \phi < 1$  exists between these domains. The interface moves into its normal direction according to the shape of the double well potential. Because the interface evolves in the direction of the lower minimum of the potential, the density function is updated based on the sensitivity analysis as in conventional steepest descent methods. As a result, the optimal shape has clear 0 or 1 domains and negligible thin phase field interface. Equation (53) is numerically solved by the semi-implicit method which is a type of finite difference method (Warren et al., 2003).

Figure 3 is about here.

## 4 Numerical Examples

The following numerical examples are provided to confirm the validity and the utility of the proposed methodology. In all examples, the piezoelectric layers are made from transversely-isotropic PZT-5H, the material properties of which are listed in Table 1. For base structures,

we use isotropic aluminum with Young's modulus  $E$  of 73[Gpa], Poisson's ratio  $\nu$  and electric conductivity  $\sigma$  of  $3.774 \times 10^7$ [S/m]. The aluminum layer also functions as an electrode. The density function  $\phi$  is only set on the piezoelectric layer, that is, we only optimize the distribution of the piezoelectric material. The optimization problem in Equations (28) and (29) is solved according to the algorithm set out in Figure 2. The penalization parameters  $p_c$ ,  $p_e$ ,  $p_\epsilon$ , and  $p_\rho$  in Equations (23)-(27) are set to 3, 3, 1, and 1, respectively. The positive coefficient  $\eta$  in Equation (55) is set to 10. At each iteration, we perform a finite element analysis of the state equation and one update of the evolution equation for the phase field function by solving the finite difference equation of the semi-implicit scheme. The time step  $\Delta t$  is set to 0.9 times the limit of the Courant number. All FEM are performed using the commercial software COMSOL Multiphysics for quick implementation of the proposed methodology, and to effectively solve the equations of state and adjoint with a multi-core processor. The frequency response problem is solved by the direct method.

Table 1 is about here.

#### 4.1 Polarization optimization of clamped circular plate

As the first benchmark example, a polarization optimization of clamped circular plate is performed, which has analytical optima discussed in (Kim et al., 2005a,b) and is used as a benchmark in (Rupp et al., 2009). Figure 4 shows a schematic diagram of the design object structure as a 25[mm] radius circular plate clamped at its edge. The top layer of the plate is composed of piezoelectric material with a thickness of 0.127[mm] and the bottom layer of aluminum with a thickness of 0.508[mm]. The upper surface of the structure is grounded. The open circuit voltage is measured between the top and bottom surfaces of the structure under a pressure of 9.65[kPa] applied to the bottom surface. As both compression and stretching stresses are applied to different parts of the piezoelectric layer, the circuit should be separated to avoid cancellation of the electric field. The distance between the circuit border and the center is represented as  $r_1$ . The border is decided based on the distribution of  $s$  obtained by solving Equations (11)-(18) by FEM. A color bar is attached to the figure to provide greater clarity although  $s$  is a discrete variable having only two values  $-1$  and  $1$ . The domain is represented as being a 2D axi-symmetrical

disk discretized by  $200 \times 4$  rectangular mesh with each element treated as a first-order iso-parametric element.

Figure 4 is about here.

Figure 5 displays the resulting distribution of the variable  $s$  obtained from the Newton-Raphson method after five iterations. Since  $s$  is plotted at the Gauss point of each element, its value can be different in each element and a gray scaling can be observed as seen in the domain  $0.0152 \leq r_1 \leq 0.0196$ . We determined the border on which the polarization direction becomes reversed at the center of the gray domain, that is,  $r_1 = 0.0175$  and  $r_1/r_0 = 0.7$ . Figure 6 shows the variation of the output voltage with  $r_1/r_0$  from 0 to 1. The vertical dotted line represents the resultant position of the polarization border  $r_1/r_0 = 0.7$ . According to Figure 6, the global optima occurs at  $r_1/r_0 = 0.71$ . Although our result has about 1% error, the proposed method can be considered as having performed well at finding the optimal polarization direction.

Figures 5 and 6 are about here.

#### 4.2 Polarization and topology optimization for cantilever energy harvester

A simultaneous optimization of the polarization and the layout of the piezoelectric material is performed as the second example. The cantilever-type energy harvester shown in Figure 7 is used as design object. The device is composed of a 0.5[mm]-thick top layer of piezoelectric material and a 1.5[mm]-thick bottom layer of aluminum. A periodic displacement input is initiated from the left side (see figure) using the so-called large mass method; masses  $1 \times 10^7$ [kg] are placed at the input nodes and a unit force applied there along  $z$ -direction. The accelerations of the masses are set to 9.8[m/s<sup>2</sup>]. No displacements are set for the  $x$  and  $y$  direction. The  $1.5 \times 10^5$ [kg/m<sup>3</sup>] distributed mass is placed on the right hand edge of the structure. Ground is set on the upper side of the structure. Neither surface traction nor surface electric charge are applied to the structure. In this type of energy harvester, the first vibrational mode, having only one anti-node domain, is usually used for power generation, as oscillations at higher frequencies having two or more anti-node domains are impractical. However, these vibrational modes are taken into consideration in this example as a numerical benchmark for

the proposed method. In the higher vibrational modes, the polarization optimization is required to avoid the cancellation of electric field, in similar manner to the first example. The piezoelectric material layer and the substrate layer are discretized by  $100 \times 50 \times 1$  and  $100 \times 50 \times 2$  cuboid meshes respectively. Each element forms a first-order iso-parametric element. To reduce computational demands, the variable  $s$  in Equation (10) is fixed to  $1 \times 10^{-3}$  at the position where  $|\varepsilon e_z|$  is less than 1% of the average value of  $|\varepsilon e_z|$ . Three iterations within the Newton-Raphson method are performed to solve the state equations in each optimization iteration. The volume constraint is set to 60% of the total volume of the piezoelectric layer.

Figure 7 is about here.

Note that the proposed method can not specify the mode shape and the corresponding harmonic frequency of the resulting optimal structure because we treated only the electromechanical coupling factor as the objective function. However, because the base plate layer has three times the thickness of the piezoelectric layer, the harmonic frequency of the whole structure will not change significantly. Thus, based on the frequency response of the initial structure, the preferred modal shapes for energy harvesting need to be determined, and the corresponding harmonic frequency estimated. We use the two types of structures for which the density functions  $\rho$  of the piezoelectric material are uniformly set to 1 or 0.1, and the variable  $s$  set to 1 over the whole domain. The structure shall be referred to as the “fully-covered structure” hereafter. Figure 8 shows the strain energy for each structure subjected to an input vibration in the frequency range 500-2500[Hz]. The deformed shapes in the x-y plane at the center of piezoelectric layer associated with the three anti-node domain is also shown in this graph at the corresponding frequency. According to the results, the resonance frequency of the optimal structure operating under the target modes can be estimated to be about 1800-2000[Hz].

Figure 8 is about here.

Input vibrations at frequencies of 1800 and 2000[Hz] are used in the optimization. Figure 9 shows optimal distribution of  $\phi$  and  $s$  obtained after 50 iterations of SLP update and 20 iterations of PFM updates. According to the results, the piezoelectric layer should be divided into three parts in the domain each part corresponding to an antinode. Figure 10 shows the total

strain energy for each optimal structure over the 1750-2250[Hz] input frequency range and the deformations at the resonance frequencies. The harmonic frequencies of both structures are about 1900[Hz] and 1980[Hz] and the deformations at these harmonic frequencies are almost identical to those expected. Figure 11 plots the objective functions of each structure in the frequency range 1900-2050[Hz]. Both optimal structures display finer-tuned performances at their harmonic frequencies. The vibration characteristic of the optimal result obtained under a 2000[Hz] vibrational input is also checked. (Being similar, the result for a 1800[Hz] input is omitted.) The frequency response strain energies were plotted in Fig. 8 together with the results for the fully covered structure. The vibration characteristic of the results was similar with that for the fully covered structure with  $\rho = 1.0$ . Thus, our assumption that the vibration characteristic of the structure is not sensitive to the piezoelectric layer layout is valid.

Figures 9, 10 and 11 are about here.

Finally, the performance of the proposed method is compared with that for conventional topology optimizations of piezoelectric layers without polarization optimization. The original equations of state in Equations (1)-(6) are used for FEM in this example. The frequencies chosen for the input vibration were 1800[Hz] respectively. Figure 12 shows the optimal distribution for  $\phi$ . Blocks of piezoelectric layer are found only in parts of domain corresponding to antinodes although different parts from the previous examples with polarization optimization.

Table 2 shows the performance comparison among optimal devices and the fully-covered devices with and without polarization optimization. The optimal and the fully-covered devices with optimal polarizations clearly achieved higher performances than those without optimal polarizations. The reason is clear considering that all domain parts corresponding to antinodes can be used in power generation given optimal polarization. Without polarization optimization, if electrodes connect the top and bottom of the piezoelectric layers and the vibrational mode has multiple nodes, the piezoelectric material must be located on only one side of the antinodes to avoid cancellation of power generating contributions. In contrast, by comparing optimal and fully-covered devices, both with optimal polarizations, the optimal device achieved about 86% performance with only about 53% of the piezoelectric material in the fully-covered device. The advantage of integrating polarization and topology optimizations in terms of the

effective use of the piezoelectric material has been confirmed by these results.

Figure 12 is about here.

Table 2 is about here.

#### 4.3 Polarization and topology optimization for energy harvesting skin

Our proposed method is finally applied to the design of energy harvesting skin as a numerical example of a practical device using higher-order vibration modes for energy harvesting. This numerical example is based on that reported in (Lee and Youn, 2011), that has the appearance of an aircraft skin. In (Lee and Youn, 2011), the energy harvesting skin was designed for multimodal vibrations. However, the optimization was performed for designing devices targeting single-mode vibrations in this example. Figure 13 shows the outline of the design object device. The plate is composited of a 0.5[mm] thick top layer of piezoelectric material and a 2.0[mm] bottom layer of aluminum fixed by rivet joints. At the rivet joints,  $z$ -directional periodic input displacements are actuated using the large mass method similar to previous examples. A mass  $1 \times 10^7$ [kg] is fixed at each of these points and a unit force is applied along  $z$ -direction; there are no  $x$  and  $y$  directional displacements. The accelerations of the masses are set to  $9.8$ [m/s<sup>2</sup>]. The upper side of the structure is grounded. Neither surface traction nor surface electric charge is applied to the structure. From symmetry considerations, only half of the design domain is modeled. Both piezoelectric material and substructure layers are discretized by  $120 \times 50 \times 1$  and  $120 \times 50 \times 2$  cuboids meshes respectively. Again each element forms a first-order iso-parametric element. Again, to reduce computational demands,  $s$  is set to  $1 \times 10^{-3}$  under the same conditions stated previously. Three iterative calculation of the Newton-Raphson method are needed performed to solve the state equations in each optimization iteration. The volume is restricted to 60% of the total volume of the piezoelectric layer.

Figure 13 is about here.

The design procedure is as the same with the previous cantilever example. The target vibration modes are first determined. Similar to the previous example, because the base plate layer has four times the thickness of the piezoelectric layer, the harmonic frequency of the whole structure will not change significantly. Figure 14 shows the frequency responses over the range 500-3000[Hz] of the fully-covered device with the same density function  $\phi$  for the piezoelectric material set above. The two target deformations are shown, the arrows pointing to the respective resonance frequencies; these modes are referred to as modes A and B. From the results, the resonance frequency with mode A and B were estimated to be about 1100-1300[Hz] and 2500-2700[Hz].

Figure 14 is about here.

For the device operating with a mode A resonance, an optimization was performed under 1050 and 1200[Hz] input vibrations; for the mode B, input vibrations were 2600 and 2700[Hz]. Figure 15 shows optimal distributions of  $\phi$  and  $s$  obtained after 50 iterations of SLP update and 20 iterations of PFM update for each input frequency. The piezoelectric material is located on antinodes in the domain and  $s$  has different sign in each domain, similar with the cantilever example. The total strain energies at each frequency and the modal shapes at the harmonic frequencies are shown in Figure 16(a) and (b). The resonances occurred at a frequency of about 1140[Hz] with the mode A device in both optimal configurations. With the mode B, the resonances occurred at about 2520[Hz] and 2580[Hz]. Figures 17(a) and (b) plot the frequency variation for objective functions for each frequency near the harmonic frequencies. The result for the fully-covered structure is omitted here as it has quite a large value. All optimal devices in each frequency range achieved similar performances. The vibration characteristics of the optimal results obtained under 1050[Hz] and 2700[Hz] input vibrations are also checked. (Other results are omitted as being similar.) The frequency response strain energies were plotted in Fig. 14 together with the results of the fully covered structure. The vibration characteristics of the results were similar with those for fully covered structure. Thus, our assumption that the vibration characteristics of the structure are not sensitive to the piezoelectric layer layout is valid, the same outcome as for the cantilever example.

Figures 15, 16 and 17 are about here.

Table 3 shows a performance comparison at 1050[Hz] and 2700[Hz] input frequencies for the resulting topology-optimized devices and the fully-covered devices with and without polarization optimization. The topology-optimized device clearly achieved higher performances than the fully-covered device without optimal polarizations. Moreover, this exceeded even the fully-covered device with optimal polarization, in contrast to the previous cantilever-type device. As shown in Figure 14, the deformations covered a wider domain that also included nodes, compared to the cantilever-type device. This is due to the rivet joint connection around the structure. Thus, in the fully-covered structure, the piezoelectric material can lie redundant even if the polarization is optimized. Moreover, the excess piezoelectric material makes the structure stiffer because of an anti-piezoelectric effect. Thus, this numerical example confirms the effectiveness of the proposed method in designing energy harvesting skins.

Table 3 is about here.

## 5 Conclusion

We have proposed a geometrical optimization method for piezoelectric energy harvesters using higher-order vibrational modes. Modified equations of state, for which the sign of the piezoelectric tensor depends on the direction of polarization, were established so that optimal poling directions can be found while avoiding cancellations of the electric fields due to opposite polarizations in the same circuit. The modified equations of state are nonlinear partial differential equations that are solved by FEM. Combining this methodology with the conventional SIMP method for piezoelectric material, an optimization method has been developed for designing the piezoelectric material layout and polarization direction. Updating the density function of the SIMP method was performed based on sensitivity analysis, the sequential linear programming (SLP) and the phase field method (PFM). The numerical examples provided illustrate the validity and utility of the proposed methodology.

The optimal topology and poling directions obtained can be implemented by ordinary means. Because the energy harvesting skin is built by attaching a piezoelectric plate on the surface of the vibrating device, the optimal result can be actualized by cutting the plate according to the optimal shape and attaching it face-up or down in accordance with the optimal poling direction. Although the generating power is lower, PolyVinylidene

DiFluoride (PVDF) piezoelectric film could make manufacturing easier.

This methodology was considered to be especially effective designing the device using complicated vibrational modes such as those used in energy harvesting skins (Lee and Youn, 2011). As shown by this example, to find the optimal location of piezoelectric material is important to improve device performance and reduce the total use and cost of the material. To perform also topology optimizations under various vibrations with complicated deformations, the poling direction must be optimized at each iteration. The proposed method obtained approximated optimal directions using nonlinear FEM.

Following on from the work described in this paper, there are some opportunities for further research. First, we ignored for simplicity sake some important factors of the vibration-based energy harvesting in the numerical examples. These factors include adjusting the harmonic frequency to the specified frequency of the input vibration, constructing a closed circuit and finding optimal value of the resistor, and a parametrical study of some geometrical size; these are basic important design considerations for energy harvesting devices. Moreover, the currently proposed methodology cannot apply if eigenfrequencies are repeated near the target frequency. To confirm the utility of the proposed method in the design of energy harvesters, we require the simultaneous optimization of the poling direction, the layout of the piezoelectric material, and the above-mentioned factors.

Second, aside from the structural problem, the electric circuit or its controls affect strongly the performance of the energy harvester (Makihara et al., 2006). Although only the open circuit model has been considered, the optimization should be performed based on real circuit settings so that realistically-designed devices can be studied.

## References

- G. Allaire. *Shape Optimization by the Homogenization Method*. Springer-Verlag, New York, 2001.
- G. Allaire. *Conception Optimale De Structures*. Springer-Verlag, Berlin, 2007.
- G. Allaire, F. Jouve, and A. M. Toader. Structural optimization using sensitivity analysis and a level-set method. *J. Comput. Phys.*, 194(1):363–393, 2004.
- S. R. Anton and H. A. Sodano. A review of power harvesting using piezoelectric materials (2003–2006). *Smart Mater. Struct.*, 16:R1, 2007.
- S. P. Beeby, M. J. Tudor, and N. M. White. Energy harvesting vibration sources for microsystems applications. *Meas. Sci. Technol.*, 17:R175, 2006.

- T. Belytschko, W. K. Liu, and B. Moran. *Nonlinear Finite Elements for Continua and Structures*. Wiley, Chichester, 2000.
- M. P. Bendsøe. Optimal shape design as a material distribution problem. *Struct. Optim.*, 1(4):193–202, 1989.
- M. P. Bendsøe and N. Kikuchi. Generating optimal topologies in structural design using a homogenization method. *Comput. Meth. Appl. Mech. Eng.*, 71(2):197–224, 1988.
- M. P. Bendsøe and O. Sigmund. Material interpolation schemes in topology optimization. *Arch. Appl. Mech.*, 69(9):635–654, 1999.
- M. P. Bendsøe and O. Sigmund. *Topology Optimization: Theory, Methods, and Applications*. Springer-Verlag, Berlin, 2003.
- D. A. Berlincourt, D. R. Curran, and H. Jaffe. Piezoelectric and piezomagnetic materials and their function in transducers. In : *Physical acoustics, Principle and methods. Vol.1, Part A*, W. P. Mason, Ed, Academic Press, pages 169–270, 1964.
- R.I. Bourisli and M.A. Al-Ajmi. Optimization of smart beams for maximum modal electromechanical coupling using genetic algorithms. *J. Intell. Mater. Syst. Struct.*, 21(9):907–914, 2010.
- T. E. Bruns, O. Sigmund, and D. A. Tortorelli. Numerical methods for the topology optimization of structures that exhibit snap-through. *Int. J. Numer. Meth. Eng.*, 55(10):1215–1237, 2002.
- S. Chen, S. Gonella, W. Chen, and W. K. Liu. A level set approach for optimal design of smart energy harvesters. *Comput. Meth. Appl. Mech. Eng.*, 199(37-40):2532–2543, 2010.
- K. A. Cook-Chennault, N. Thambi, and A. M. Sastry. Powering mems portable devices - a review of non-regenerative and regenerative power supply systems with special emphasis on piezoelectric energy harvesting systems. *Smart Mater. Struct.*, 17:043001, 2008.
- N. E. duToit, B. L. Wardle, and S. G. Kim. Design considerations for mems-scale piezoelectric mechanical vibration energy harvesters. *Integrated Ferroelectrics*, 71:121–160, 2005.
- A. Erturk and D. J. Inman. A distributed parameter electromechanical model for cantilevered piezoelectric energy harvesters. *J. Vib. Acoust.*, 130:041002, 2008a.
- A. Erturk and D.J. Inman. On mechanical modeling of cantilevered piezoelectric vibration energy harvesters. *J. Intell. Mater. Syst. Struct.*, 19(11):1311–1325, 2008b.
- A. Erturk, P. A. Tarazaga, J. R. Farmer, and D. J. Inman. Effect of strain nodes and electrode configuration on piezoelectric energy harvesting from cantilevered beams. *J. Vib. Acoust.*, 131:011010, 2009.
- S. Gonella, A.C. To, and W.K. Liu. Interplay between phononic bandgaps and piezoelectric microstructures for energy harvesting. *J. Mech. Phys. Solid.*, 57(3):621–633, 2009.
- J. E. Kim, D. S. Kim, P. S. Ma, and Y. Y. Kim. Multiphysics interpolation for the topology optimization of piezoelectric systems. *Comput. Meth. Appl. Mech. Eng.*, 199(49-52):3153–3168, 2010.
- S. Kim, W. W. Clark, and Q. M. Wang. Piezoelectric energy harvesting with a clamped circular plate: analysis. *J. Intell. Mater. Syst. Struct.*, 16(10):847–854, 2005a.
- S. Kim, W.W. Clark, and Q.M. Wang. Piezoelectric energy harvesting with a clamped circular plate: experimental study. *J. Intell. Mater. Syst. Struct.*, 16(10):855–863, 2005b.
- M. Kögl and E.C.N. Silva. Topology optimization of smart structures: design of piezoelectric plate and shell actuators. *Smart Mater. Struct.*, 14:387–399, 2005.
- L. D. Landau, L. P. Pitaevskii, and E.M. Lifshitz. *Electrodynamics of Continuous Media, Second Edition*. Butterworth-Heinemann, Oxford, 1984.
- C. Lee and J. Xie. Design and optimization of wafer bonding packaged microelectromechanical systems thermoelectric power generators with heat dissipation path. *J. Vac. Sci. Technol. B*, 27:1267–1271, 2009.
- S. Lee and B. D. Youn. A new piezoelectric energy harvesting design concept: multimodal energy harvesting skin. *IEEE Trans. Ultrason. Ferroelectrics. Freq. Contr.*, 58(3):629–645, 2011.
- S. Lee, B.D. Youn, and B.C. Jung. Robust segment-type energy harvester and its application to a wireless sensor. *Smart Mater. Struct.*, 18:095021, 2009.
- K. Makiyara, J. Onoda, and T. Miyakawa. Low energy dissipation electric circuit for energy harvesting. *Smart Mater. Struct.*, 15:1493, 2006.
- P. H. Nakasone and E. C. N. Silva. Dynamic design of piezoelectric laminated sensors and actuators using topology optimization. *J. Intell. Mater. Syst. Struct.*, 21(16):1627–1652, 2010.
- S. Priya. Advances in energy harvesting using low profile piezoelectric transducers. *J. Electroceram.*, 19(1):167–184, 2007.
- S. Roundy, P.K. Wright, and J. Rabaey. A study of low level vibrations as a power source for wireless sensor nodes. *Comput. Comm.*, 26(11):1131–1144.
- C.J. Rupp, A. Evgrafov, K. Maute, and M.L. Dunn. Design of piezoelectric energy harvesting systems: A topology optimization approach based on multilayer

- plates and shells. *J. Intell. Mater. Syst. Struct.*, 20(16):1923–1939, 2009.
- H.A. Sodano, D.J. Inman, and G. Park. A review of power harvesting from vibration using piezoelectric materials. *Shock Vib. Digest*, 36(3):197–206, 2004.
- K. H. Sun and Y. Y. Kim. Layout design optimization for magneto-electro-elastic laminate composites for maximized energy conversion under mechanical loading. *Smart Mater. Struct.*, 19:055008, 2010.
- Y. Tadesse, S. Zhang, and S. Priya. Multimodal energy harvesting system: piezoelectric and electromagnetic. *J. Intell. Mater. Syst. Struct.*, 20(5):625–623, 2009.
- A. Takezawa, S. Nishiwaki, and M. Kitamura. Shape and topology optimization based on the phasefield method and sensitivity analysis. *J. Comput. Phys.*, 229(7):2697–2718, 2010.
- M. Y. Wang, X. Wang, and D. Guo. A level set method for structural topology optimization. *Comput. Meth. Appl. Mech. Eng.*, 192(1-2):227–246, 2003.
- J. A. Warren, R. Kobayashi, A. E. Lobkovsky, and W. Craig Carter. Extending phase field models of solidification to polycrystalline materials. *Acta Mater.*, 51(20):6035–6058, 2003.
- B. Zheng, C. J. Chang, and H. C. Gea. Topology optimization of energy harvesting devices using piezoelectric materials. *Struct. Multidisc. Optim.*, 38(1):17–23, 2009.
- M. Zhou and G. I. N. Rozvany. The coc algorithm. ii: Topological, geometrical and generalized shape optimization. *Comput. Meth. Appl. Mech. Eng.*, 89(1-3):309–336, 1991.

## Appendix

In this appendix, the detailed derivation of the sensitivity in Equation (30) and the adjoint equations in Equations (32)-(35) is outlined. The derivatives of the objective functions with respect to the density function are based on the procedure shown in Chapter 5 of (Allaire, 2007). The general objective function of piezoelectric problem is defined as  $J(\phi) = \int j(\mathbf{u}, V)dx$ . The derivative of this function in the direction  $\theta$  is then

$$\begin{aligned} \langle J'(\phi), \theta \rangle &= \int j'(\mathbf{u}) \langle \mathbf{u}'(\phi), \theta \rangle dx + \int j'(V) \langle V'(\phi), \theta \rangle dx \\ &= \int j'(\mathbf{u}) \mathbf{v} dx + \int j'(V) w dx \end{aligned} \quad (57)$$

where  $\mathbf{v} = \langle \mathbf{u}'(\phi), \theta \rangle$ ,  $w = \langle V'(\phi), \theta \rangle$ . Setting adjoint states  $\mathbf{p}$  and  $q$  as test functions of the weak-form equations of state in Equations (11)-(18), the Lagrangian is

formulated as follows:

$$\begin{aligned} L(\phi, \mathbf{u}, V, \mathbf{p}, q) &= \int j(\mathbf{u}, V) dx - m(\mathbf{u}, \mathbf{p}) + a(\mathbf{u}, \mathbf{p}) - b(\mathbf{p}, V) - L_m(\mathbf{p}) \\ &\quad + b(\mathbf{u}, q) + c(V, q) - L_e(q). \end{aligned} \quad (58)$$

Using this, the derivative of the objective function can be expressed as

$$\begin{aligned} \langle j'(\phi), \theta \rangle &= \left\langle \frac{\partial L}{\partial \phi}(\phi, \mathbf{u}, V, \mathbf{p}, q), \theta \right\rangle + \left\langle \frac{\partial L}{\partial \mathbf{u}}(\phi, \mathbf{u}, V, \mathbf{p}, q), \langle \mathbf{u}'(\phi), \theta \rangle \right\rangle \\ &\quad + \left\langle \frac{\partial L}{\partial V}(\phi, \mathbf{u}, V, \mathbf{p}, q), \langle V'(\phi), \theta \rangle \right\rangle \\ &= \left\langle \frac{\partial L}{\partial \phi}(\phi, \mathbf{u}, V, \mathbf{p}, q), \theta \right\rangle + \left\langle \frac{\partial L}{\partial \mathbf{u}}(\phi, \mathbf{u}, V, \mathbf{p}, q), \mathbf{v} \right\rangle \\ &\quad + \left\langle \frac{\partial L}{\partial V}(\phi, \mathbf{u}, V, \mathbf{p}, q), w \right\rangle. \end{aligned} \quad (59)$$

Consider the case where the second and third terms are zero. These terms are calculated as follows:

$$\left\langle \frac{\partial L}{\partial \mathbf{u}}, \mathbf{v} \right\rangle = \int j'(\mathbf{u}) \mathbf{v} dx - m(\mathbf{v}, \mathbf{p}) + a(\mathbf{v}, \mathbf{p}) + b(\mathbf{v}, q) = 0, \quad (60)$$

$$\left\langle \frac{\partial L}{\partial V}, w \right\rangle = \int j'(V) w dx - b(p, w) + c(w, q) = 0. \quad (61)$$

When the adjoint states  $\mathbf{p}$  and  $q$  satisfy the above adjoint equations, the second and third terms of Equation (59) can be ignored. On the other hand, the derivatives of Equations (11) - (18) with respect to  $\phi$  in the direction  $\theta$  are

$$\begin{aligned} -m'(\mathbf{u}, \mathbf{p}) - m(\mathbf{v}, \mathbf{p}) + a'(\mathbf{u}, \mathbf{p}) + a(\mathbf{v}, \mathbf{p}) \\ -b'(\mathbf{p}, V) - b(\mathbf{p}, w) = 0 \end{aligned} \quad (62)$$

$$b'(\mathbf{u}, q) + b(\mathbf{p}, q) + c'(V, q) + c(w, q) = 0 \quad (63)$$

where

$$m'(\mathbf{u}, \mathbf{p}) = \omega_{\text{input}}^2 \int_{\Omega} \rho'(\phi) \mathbf{u} \mathbf{p} \theta dx \quad (64)$$

$$a'(\mathbf{u}, \mathbf{p}) = \int_{\Omega} \boldsymbol{\varepsilon}(\mathbf{u})^T \mathbf{C}'(\phi) \boldsymbol{\varepsilon}(\mathbf{p}) \theta dx \quad (65)$$

$$b'(\mathbf{p}, V) = \int_{\Omega} \boldsymbol{\varepsilon}(\mathbf{p})^T \mathbf{e}'_s(\phi) \mathbf{E}(V) \theta dx \quad (66)$$

$$c'(V, q) = \int_{\Omega} \mathbf{E}(V)^T \boldsymbol{\epsilon}'(\phi) \mathbf{E}(q) \theta dx. \quad (67)$$

Substituting Equations (62) and (63) into Equations (60) and (61) and combining them into one equation, the following equation is obtained:

$$\begin{aligned} & \int j'(\mathbf{u})\mathbf{v}dx + \int j'(V)w dx \\ &= -m'(\mathbf{u}, \mathbf{p}) + a'(\mathbf{u}, \mathbf{p}) - b'(p, V) + b'(\mathbf{u}, q) + c'(V, q) \end{aligned} \quad (68)$$

Substituting Equation (68) into Equation (57) yields following equation:

$$\begin{aligned} J'(\phi) &= -\omega_{\text{input}}^2 \rho'(\phi) \mathbf{u} \mathbf{p} \\ &+ \boldsymbol{\varepsilon}(\mathbf{u})^T \mathbf{C}'(\phi) \boldsymbol{\varepsilon}(\mathbf{p}) - \boldsymbol{\varepsilon}(\mathbf{p})^T \mathbf{e}'_s(\phi) \mathbf{E}(V) \\ &+ \boldsymbol{\varepsilon}(\mathbf{u})^T \mathbf{e}'_s(\phi) \mathbf{E}(q) - \mathbf{E}(V)^T \boldsymbol{\epsilon}'(\phi) \mathbf{E}(q). \end{aligned} \quad (69)$$

Next, the adjoint equations are calculated from Equations (60) and (61). When the electric energy  $c(V, V)$  is considered as the objective function, it is formulated as follows:

$$\begin{aligned} J(\rho) &= \int j(\mathbf{u}, V) dx \\ &= c(V, V). \end{aligned} \quad (70)$$

Thus,

$$\int j'(\mathbf{u})\mathbf{v}dx = 0 \quad (71)$$

$$\int j'(V)w dx = 2c(V, w) \quad (72)$$

Substituting Equations (71) and (72) into Equations (60) and (61) respectively gives following equation

$$m(\mathbf{v}, \mathbf{p}) - a(\mathbf{v}, \mathbf{p}) - b(\mathbf{v}, q) = 0 \quad (73)$$

$$b(p, w) + c(w, q) = 2c(V, w) \quad (74)$$

When the strain energy  $a(\mathbf{u}, \mathbf{u})$  is considered as the objective function, it is formulated as follows:

$$\begin{aligned} J(\rho) &= \int j(\mathbf{u}, V) dx \\ &= a(\mathbf{u}, \mathbf{u}) \end{aligned} \quad (75)$$

Thus,

$$\int j'(\mathbf{u})\mathbf{v}dx = 2a(\mathbf{u}, \mathbf{v}) \quad (76)$$

$$\int j'(V)w dx = 0 \quad (77)$$

Substituting Equations (76) and (77) into Equations (60) and (61) respectively gives following equation

$$2a(\mathbf{u}, \mathbf{v}) - m(\mathbf{p}, \mathbf{v}) + a(\mathbf{p}, \mathbf{v}) + b(\mathbf{v}, q) = 0 \quad (78)$$

$$-b(\mathbf{p}, w) + c(q, w) = 0. \quad (79)$$

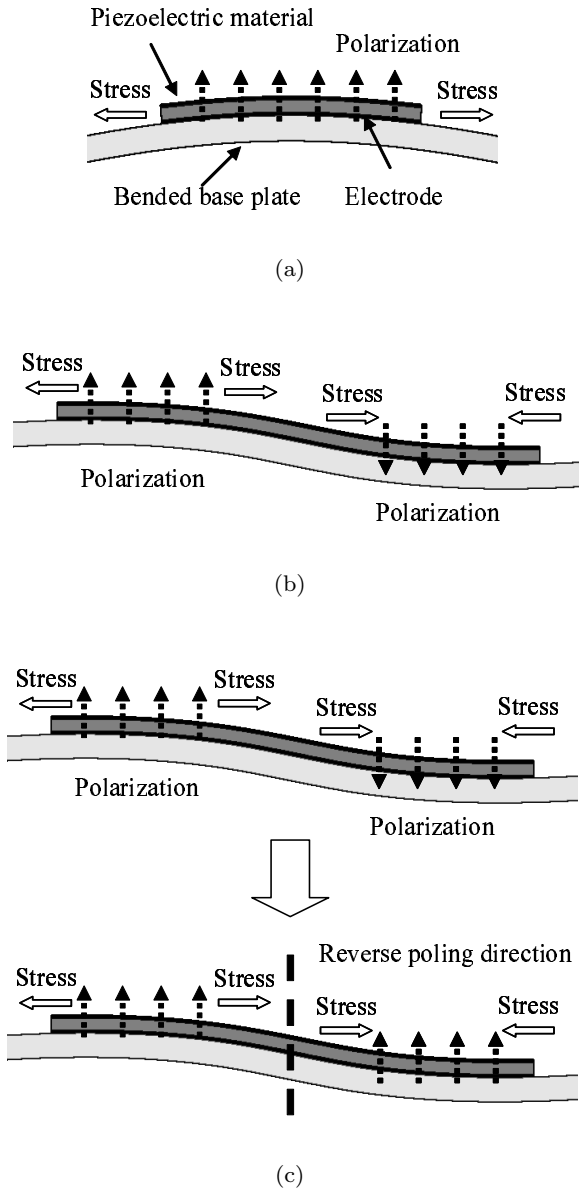


**Fig. 1** Cross-sectional view of the deformed cantilever-type energy harvester. (a) With uni-directional polarization. (b) With bi-directional polarization. (c) Reversing poling direction to avoid cancellation of the electric field

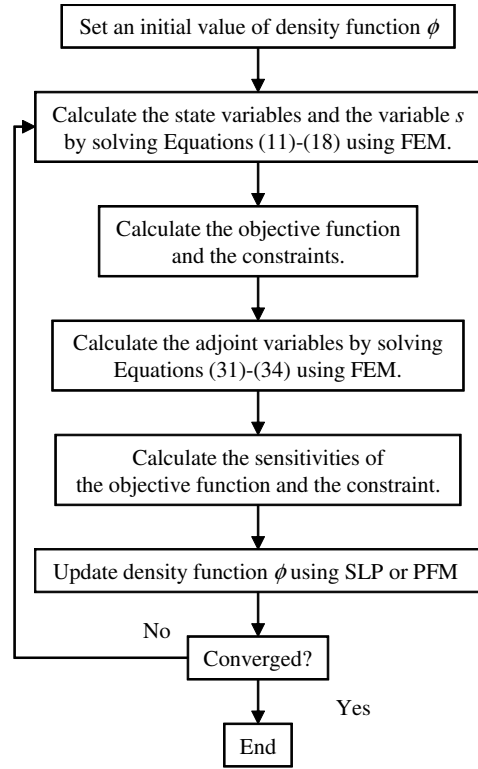


**Fig. 2** Flowchart of the optimization algorithm

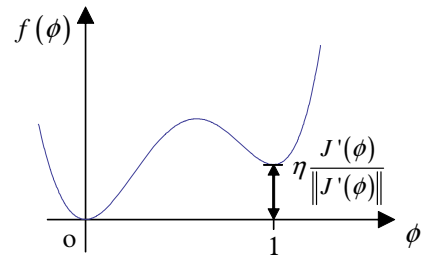


**Fig. 3** The outline of the double well potential used in PFM

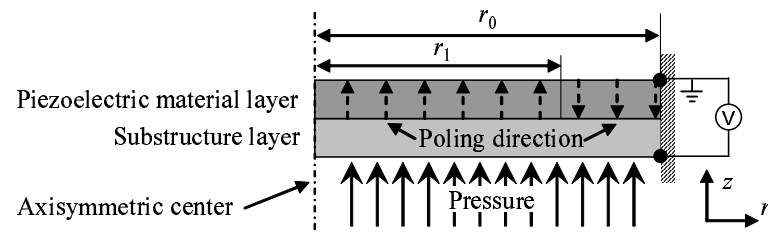


**Fig. 4** Cross-section view of the clamped circular energy harvester

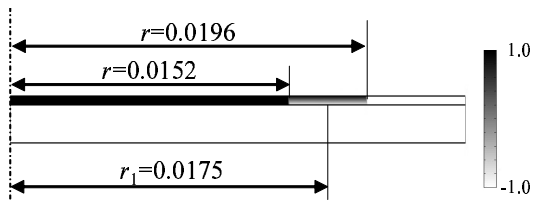


**Fig. 5** Optimal distribution of  $s$  and analyzed polarization border

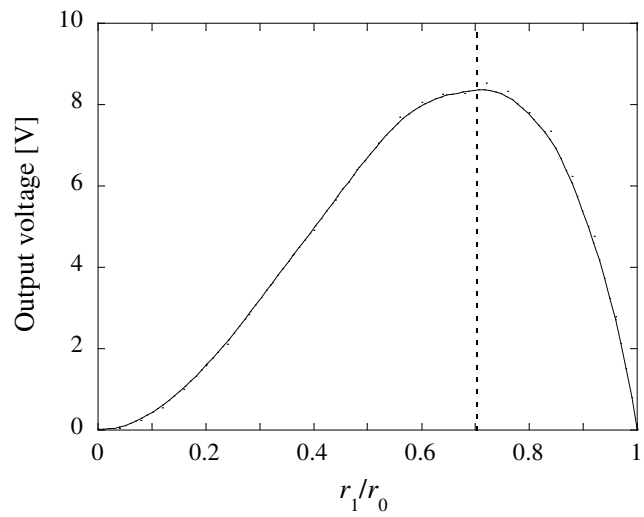


**Fig. 6** The relationship between the output voltage and the ratio  $r_1/r_0$

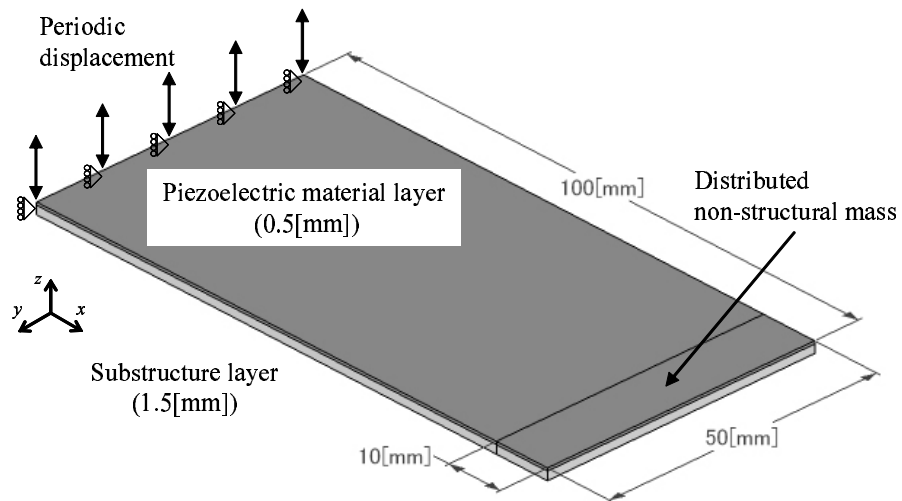


**Fig. 7** Design object structure of cantilever type energy harvester

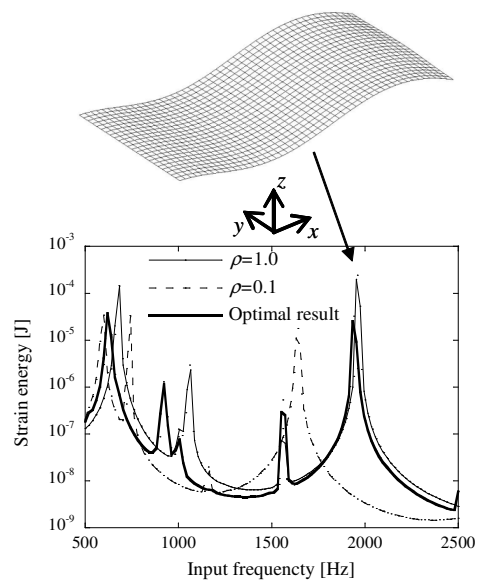


**Fig. 8** Total strain energy of the fully covered structures and an optimal result under 500-2500[Hz] input vibrations. The optimal result was obtained under 2000[Hz] input vibration.

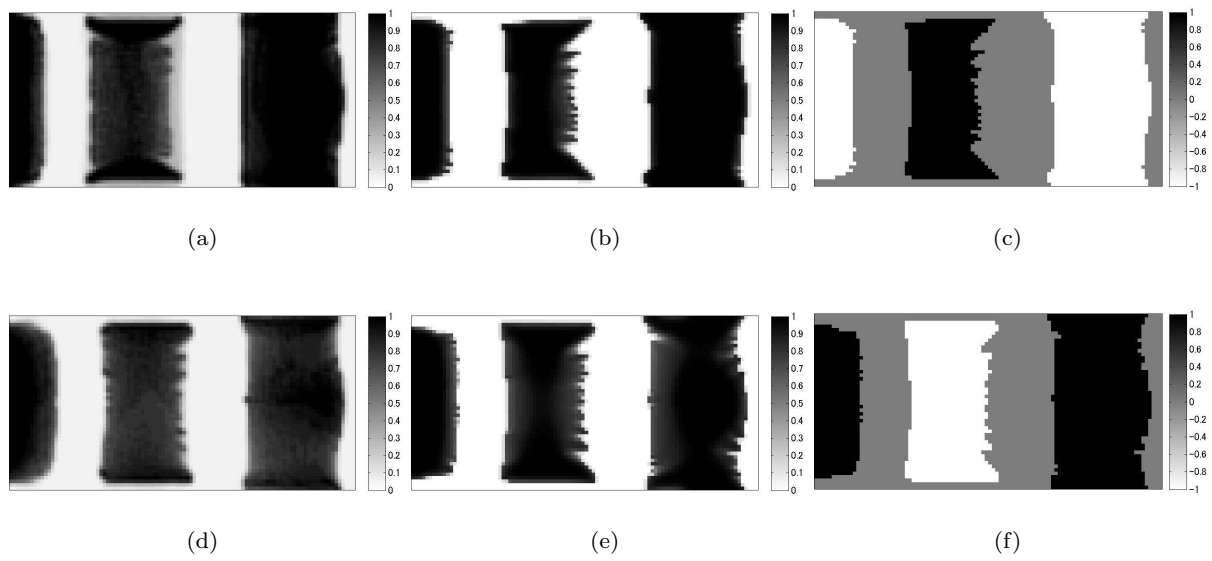


**Fig. 9** Optimal distributions of  $\phi$  and  $e$ . (a)  $\phi$  of 1800[Hz] input after SLP update. (b)  $\phi$  of 1800[Hz] input after PFM update. (c)  $e$  of 1800[Hz] input after PFM update. (d)  $\phi$  of 2000[Hz] input after SLP update. (e)  $\phi$  of 2000[Hz] input after PFM update. (f)  $e$  of 2000[Hz] input after PFM update.

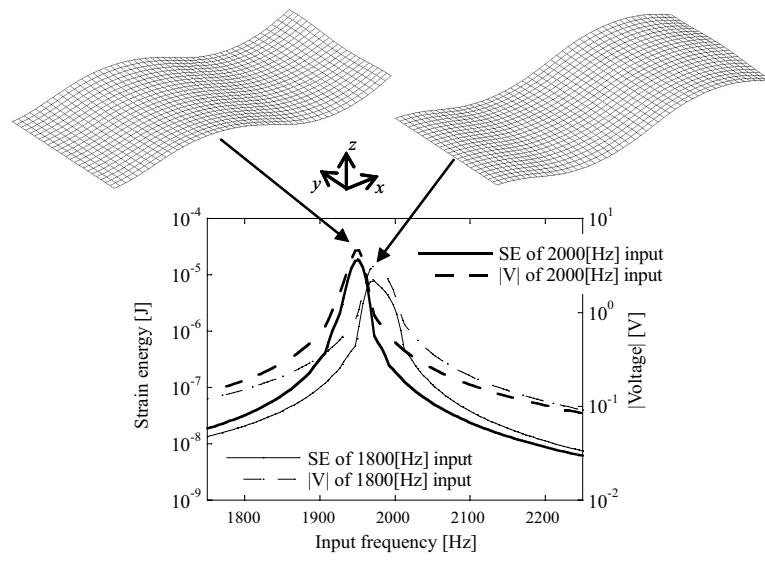


**Fig. 10** Total strain energy of each optimal structure under 1750-2250[Hz] input vibration.

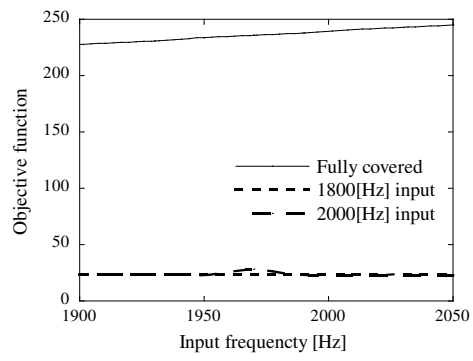


**Fig. 11** Objective function of each optimal structure and fully covered structure under 1900-2050[Hz] input vibration.

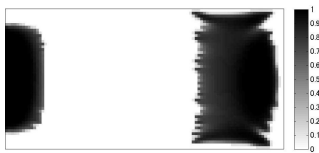


**Fig. 12** 2000[Hz] input optimal distributions of  $\phi$  without polarization optimization.

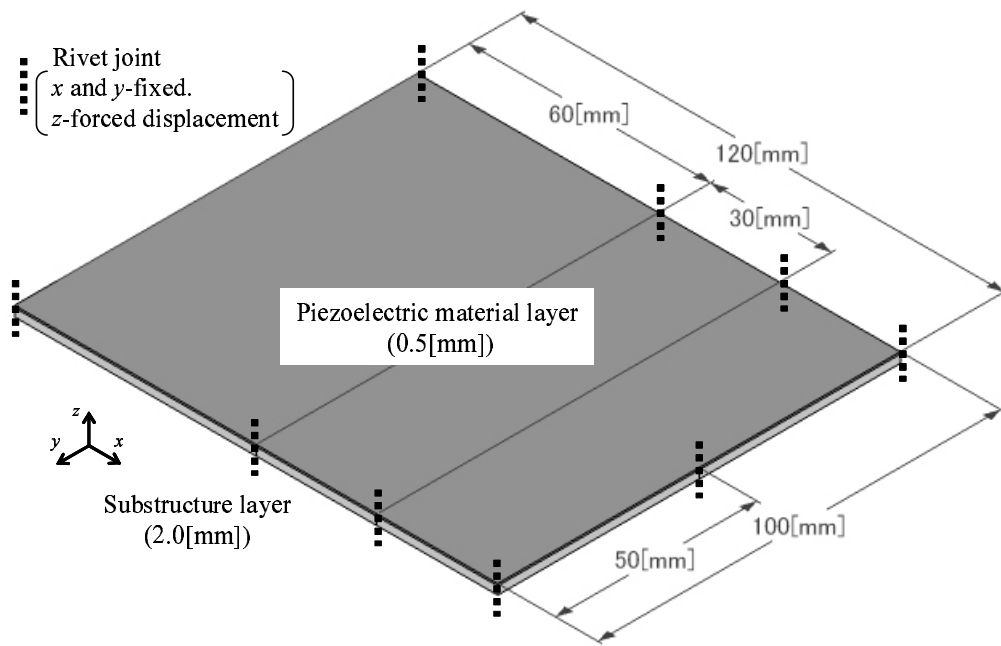


**Fig. 13** Design object structure of an energy harvesting skin.

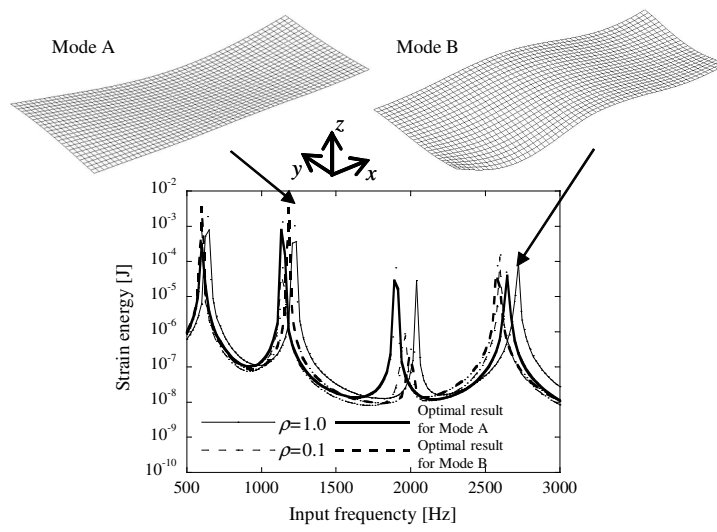


**Fig. 14** Total strain energy of the fully covered structures and optimal results under 500-3000[Hz] input vibrations. Optimal results for Mode A and B were obtained under 1050[Hz] and 2700[Hz] inputs respectively.

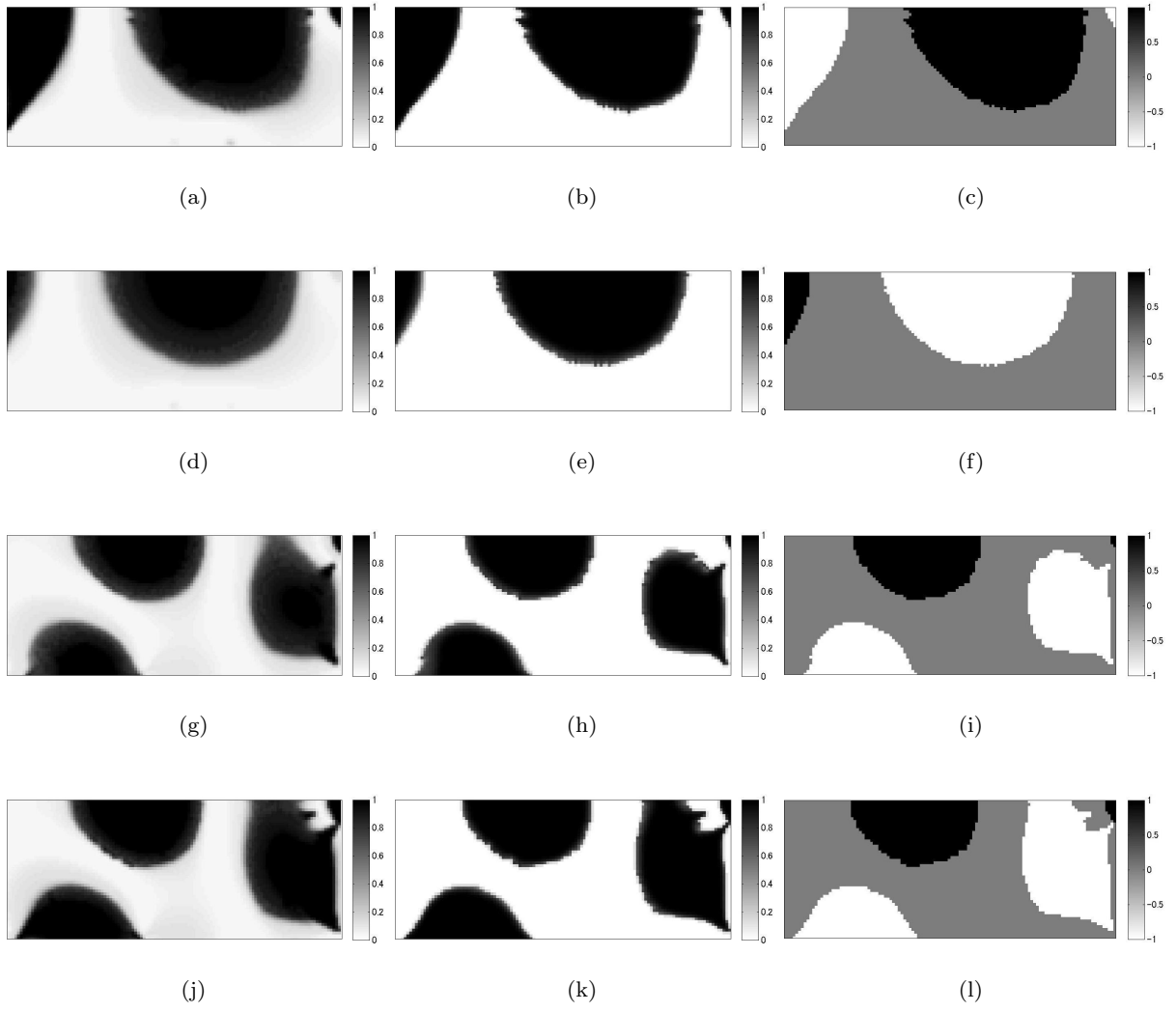


**Fig. 15** Optimal distributions of  $\phi$  and  $s$ . (a)  $\phi$  of 1050[Hz] input. (b)  $s$  of 1050[Hz] input. (c)  $\phi$  of 1200[Hz] input. (d)  $s$  of 1200[Hz] input. (e)  $\phi$  of 2600[Hz] input. (f)  $s$  of 2600[Hz] input. (g)  $\phi$  of 2700[Hz] input. (h)  $s$  of 2700[Hz] input.

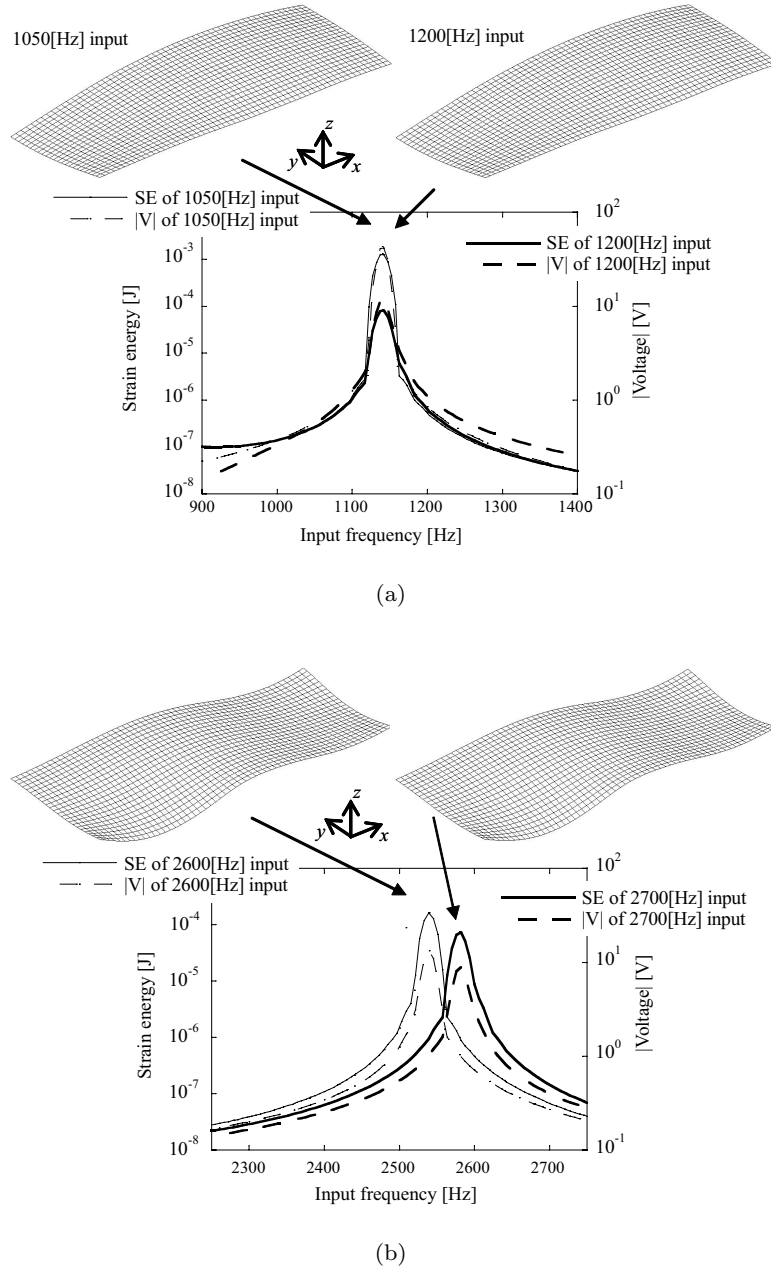
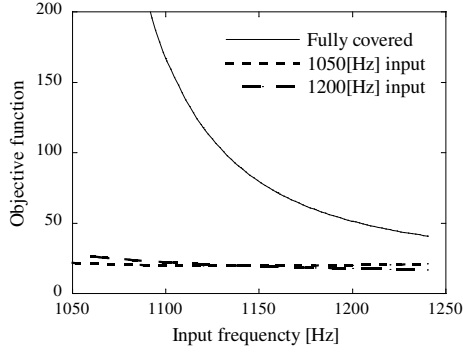
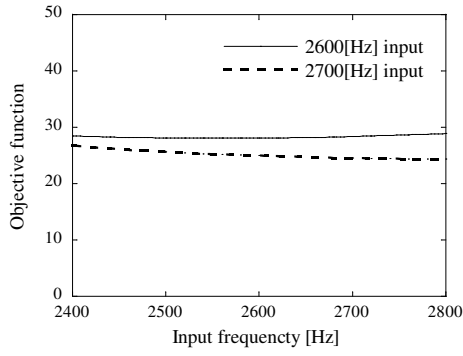


**Fig. 16** Total strain energy of each optimal structure. (a) For the mode A under 900-1400[Hz] input vibration. (b) For the mode B under 2250-2750[Hz] input vibration.



(a)



(b)

**Fig. 17** Objective function of each optimal structure. (a) For the mode A under 1050-1250[Hz] input vibration. (b) For the mode B under 2400-2800[Hz] input vibration.

**Table 1** Material properties of transversely-isotropic PZT-5H

$C_{11} = 127.2[\text{GPa}]$	$e_{31} = -6.6[\text{C/m}^2]$
$C_{12} = 80.2[\text{GPa}]$	$e_{33} = 23.2[\text{C/m}^2]$
$C_{13} = 84.7[\text{GPa}]$	$e_{15} = 17.0[\text{C/m}^2]$
$C_{33} = 117.4[\text{GPa}]$	$\varepsilon_{r11} = 1704.4$
$C_{44} = 23.0[\text{GPa}]$	$\varepsilon_{r22} = 1704.4$
$C_{66} = 23.5[\text{GPa}]$	$\varepsilon_{r33} = 1433.6$
Permittivity $\varepsilon = \varepsilon_r \varepsilon_0$ with $\varepsilon_0 = 8.854 \times 10^{-12}[\text{F/m}]$	
Mass density $\rho = 7500[\text{kg/m}^3]$	

**Table 2** Performance comparison of the topology optimized and the fully covered devices

	Harmonic frequency with the specified mode [Hz]	Electromechanical coupling coefficient [%]	Volume [mm <sup>3</sup> ]
Topology optimization			
with polarization optimization	1960	4.3	1428
without polarization optimization	1920	3.1	941
Fully covered			
with polarization optimization	2040	4.9	2500
without polarization optimization	1960	0.4	2500

**Table 3** Performance comparison of the topology optimized and the fully covered devices

		Harmonic frequency with the specified mode [Hz]	Electromechanical coupling coefficient[%]	Volume [mm <sup>3</sup> ]
For mode A (Input frequency 1050[Hz])	Topology optimization with polarization optimization	1140	5.1	1404
	Fully covered			
	with polarization optimization	1240	3.0	3000
	without polarization optimization	1220	2.2	3000
For mode B (Input frequency 2700[Hz])	Topology optimization with polarization optimization	2580	3.9	1423
	Fully covered			
	with polarization optimization	2800	3.7	3000
	without polarization optimization	2720	0.1	3000